REPORT

Microtubule minus-end stability is dictated by the tubulin off-rate

Claire Strothman[1], Veronica Farmer[1], Göker Arpağ[1], Nicole Rodgers[1], Marija Podolski[1], Stephen Norris[1], Ryoma Ohi[2], and Marija Zanic[1,3,4]

Dynamic organization of microtubule minus ends is vital for the formation and maintenance of acentrosomal microtubule arrays. In vitro, both microtubule ends switch between phases of assembly and disassembly, a behavior called dynamic instability. Although minus ends grow slower, their lifetimes are similar to those of plus ends. The mechanisms underlying these distinct dynamics remain unknown. Here, we use an in vitro reconstitution approach to investigate minus-end dynamics. We find that minus-end lifetimes are not defined by the mean size of the protective GTP-tubulin cap. Rather, we conclude that the distinct tubulin off-rate is the primary determinant of the difference between plus- and minus-end dynamics. Further, our results show that the minus-end–directed kinesin-14 HSET/KIFC1 suppresses tubulin off-rate to specifically suppress minus-end catastrophe. HSET maintains its protective minus-end activity even when challenged by a known microtubule depolymerase, kinesin-13 MCAK. Our results provide novel insight into the mechanisms of minus-end dynamics, essential for our understanding of microtubule minus-end regulation in cells.

Introduction

Microtubules are biological polymers essential for cell division, intracellular transport, and morphogenesis. These structurally polar polymers are composed of αβ-tubulin heterodimer subunits that polymerize head to tail, such that only β-tubulin is exposed at the plus end and α-tubulin at the minus end (Nogales et al., 1995; Fan et al., 1996). A quintessential feature of microtubules is their stochastic switching between phases of growth and shrinkage, called dynamic instability (Mitchison and Kirschner, 1984). Historically, studies of microtubule dynamics almost exclusively focused on microtubule plus ends, which are often highly dynamic in cells. In contrast, minus ends are often anchored at microtubule organizing centers and have, thus, been generally presumed to be nondynamic (Dammermann et al., 2003). However, many cells, including meiotic oocytes, epithelial cells, and neurons, also contain microtubule populations with "free" minus ends, (Yvon and Wadsworth, 1997; Dammermann et al., 2003; Sanchez and Feldman, 2017; Martin and Akhmanova, 2018), and even within mitotic spindles where microtubules emanate from centrosomes, large populations of minus ends remain uncapped by γ-tubulin (O'Toole et al., 2003; Redemann et al., 2017). It is therefore increasingly evident that active regulation of minus ends is key to microtubule

organization and function (Akhmanova and Hoogenraad, 2015; Akhmanova and Steinmetz, 2015; Martin et al., 2018; Martin and Akhmanova, 2018).

Early in vitro reconstitution studies demonstrated that, although both microtubule ends exhibited dynamic instability, minus ends had distinctly slower growth rates and less frequent transitions from growth to shrinkage, termed "catastrophe" (Bergen and Borisy, 1980; Mitchison and Kirschner, 1984; Horio and Hotani, 1986; Walker et al., 1988). Microtubules grow by addition of GTP-bound tubulin subunits, and incorporation of tubulin dimers into the polymer triggers GTP hydrolysis in the β-tubulin subunit after a brief delay, resulting in a "cap" of GTP-tubulin at growing microtubule ends. The process of GTP hydrolysis induces structural changes in the microtubule lattice, ultimately resulting in catastrophe if the cap is lost (Carlier and Pantaloni, 1981; Voter et al., 1991; Nogales et al., 1998; Zhang et al., 2015; Duellberg et al., 2016). Over the last few decades, a myriad of analytical and computational models of microtubule catastrophe have emerged. They range from complex descriptions involving dozens of parameters, most of which are still not experimentally tractable, to simpler ones, using kinetic rates of tubulin association, dissociation, and hydrolysis, aiming to

[1]Department of Cell and Developmental Biology, Vanderbilt University, Nashville, TN; [2]Department of Cell and Developmental Biology, University of Michigan Medical School, Ann Arbor, MI; [3]Department of Chemical and Biomolecular Engineering, Vanderbilt University, Nashville, TN; [4]Department of Biochemistry, Vanderbilt University, Nashville, TN.

Correspondence to Marija Zanic: marija.zanic@vanderbilt.edu; M. Podolski's present address is Department of Bioengineering, University of California, Berkeley, Berkeley, CA.

capture the key features of microtubule dynamics (Bowne-Anderson et al., 2013). Our models of microtubule dynamics are almost exclusively based on the plus-end behavior. For example, it is thought that the size of the GTP cap plays an essential role in plus-end stability (Duellberg et al., 2016). Furthermore, it has been shown that plus-end catastrophe is not a single-step random process; rather, the probability of catastrophe increases over time, such that microtubule plus ends effectively age (Odde et al., 1995; Gardner et al., 2011b). To what extent our understanding of plus-end dynamics applies to the minus end remains unknown.

In this study, we use biochemical in vitro reconstitution with purified protein components and total internal reflection fluorescence (TIRF) microscopy to directly interrogate minus-end dynamics. We first focus on determining the kinetic rates of tubulin assembly and the size of the stabilizing cap at minus ends in the absence of additional regulators. We then use two human mitotic kinesins, kinesin-13 MCAK and kinesin-14 HSET/KIFC1, to probe our understanding of minus-end dynamics. MCAK is an extensively studied microtubule depolymerase, which indiscriminately targets and destabilizes either microtubule end (Wordeman and Mitchison, 1995; Walczak et al., 1996; Desai et al., 1999; Moores et al., 2002; Hunter et al., 2003; Helenius et al., 2006; Benoit et al., 2018). HSET is a minus-end–directed kinesin identified to have a crucial role in focusing multipolar spindles in dividing cancer cells (Kwon et al., 2008; Wu et al., 2013; Pannu et al., 2015; Xiao and Yang, 2016; Fu et al., 2018). Effects of HSET on microtubule dynamics have not previously been studied; however, given its minus-end–directed motor activity (Case et al., 1997; Mountain et al., 1999; Norris et al., 2018; Reinemann et al., 2018), it is a promising candidate for a minus-end–specific regulator.

Results and discussion

Microtubule minus ends undergo catastrophe less frequently than plus ends, when controlling for the growth rate

To investigate the relationship between microtubule growth and catastrophe at minus ends, we used an established in vitro microtubule dynamics assay (Gell et al., 2010; Zanic, 2016). We grew dynamic microtubule extensions from guanosine-5′-[(α,β)methyleno]triphosphate (GMPCPP)–stabilized microtubule "seeds" over a range of tubulin concentrations (4–13 μM) and imaged them using TIRF microscopy. The two microtubule ends were differentiated based on their relative growth rates (Fig. 1 A). We note that, in our study, we are not aiming to measure the rapid growth fluctuations occurring on the millisecond scale due to the extremely transient association of tubulin dimers (Gardner et al., 2011a). Rather, we are interested in the kinetics of polymer-incorporated tubulin subunits. We therefore determined the tubulin on-rate at each end using a linear regression of the mean growth rates as a function of tubulin concentration (Oosawa, 1970; Fig. 1 B; see Materials and methods). We found the minus-end tubulin on-rate to be nearly four times smaller than that of the plus end (0.88 ± 0.04 μM^{-1} s^{-1} vs. 3.34 ± 0.02 μM^{-1} s^{-1}, respectively), consistent with previous reports (Bergen and Borisy, 1980; Mitchison

and Kirschner, 1984; Walker et al., 1988; O'Brien et al., 1990; Trinczek et al., 1993; Mickolajczyk et al., 2019).

Measurements of catastrophe frequency revealed an eightfold decrease over the range of 4–13 μM tubulin at the plus end (0.45 ± 0.05 min^{-1}, standard error [SE], n = 71, to 0.057 ± 0.008 min^{-1}, SE, n = 55), consistent with previous reports (Walker et al., 1988; Drechsel et al., 1992; Gardner et al., 2011b; Fig. 1 C). Minus ends were relatively stable in all of our experimental conditions and displayed only a twofold decrease in catastrophe frequency over the same range of tubulin concentrations (4–13 μM tubulin: 0.22 ± 0.06 min^{-1}, SE, n = 13, to 0.13 ± 0.01 min^{-1}, SE, n = 176; Fig. 1 C). Both ends exhibited a trend in which increasing growth rates were accompanied by a decrease in catastrophe frequency (Fig. 1 D). However, comparison of plus and minus ends growing at similar growth rates (~7 nm s^{-1}), achieved using different tubulin concentrations, revealed nearly a fourfold lower catastrophe frequency at the minus end (Fig. 1 D, shaded region). The finding that minus ends undergo catastrophe less frequently than plus ends when controlled for the growth rate emphasizes key differences in the dynamics of the two ends.

Minus-end catastrophe is not a single-step random process

One potential difference in the catastrophe mechanism at the two ends may be due to distinct aging processes, as suggested by earlier studies (Odde et al., 1995). To further explore this possibility, we measured the microtubule lifetime distributions at both ends with increased spatiotemporal resolution and larger sample sizes (n = 417–1206 lifetimes per condition) compared with the previous study (Odde et al., 1995). We found that distributions of minus-end lifetimes were well fit by a gamma function (see Materials and methods) at both low (6 μM) and high (13 μM) tubulin concentrations (Fig. 1 E and Fig. S1). None of the distributions, at either the plus or minus end, were well fit by a single-exponential function, as evidenced by the gamma function step parameters distinct from 1 (Fig. 1 E and Fig. S1). At 13 μM tubulin, minus-end lifetimes had a step parameter of 2.3 ± 0.3 (95% confidence interval [CI]). Furthermore, the comparison of gamma fit parameters at plus and minus ends growing with 6 μM tubulin revealed similar step parameters (minus: 2.0 ± 0.2 [95% CI]; plus: 1.7 ± 0.1 [95% CI]; Fig. S1). We conclude that like plus ends, minus ends also undergo aging, and that a distinct aging process at the minus end is not the cause of the observed differences in dynamics between the two ends.

Microtubule minus ends have small cap sizes, set by slow growth rate

Next, we considered whether distinct dynamics at the two ends could be explained by the relative size of their stabilizing caps. The size of the GTP cap is set by the difference in the microtubule growth rate and the GTP hydrolysis rate (see Materials and methods) and can be inferred by localization of EB-family proteins, which recognize the nucleotide state of tubulin and display a "comet"-like localization at growing microtubule ends (Zanic et al., 2009; Maurer et al., 2012; Seetapun et al., 2012; Zhang et al., 2015). Previous studies of microtubule plus ends found that the EB-comet size increased with the increasing
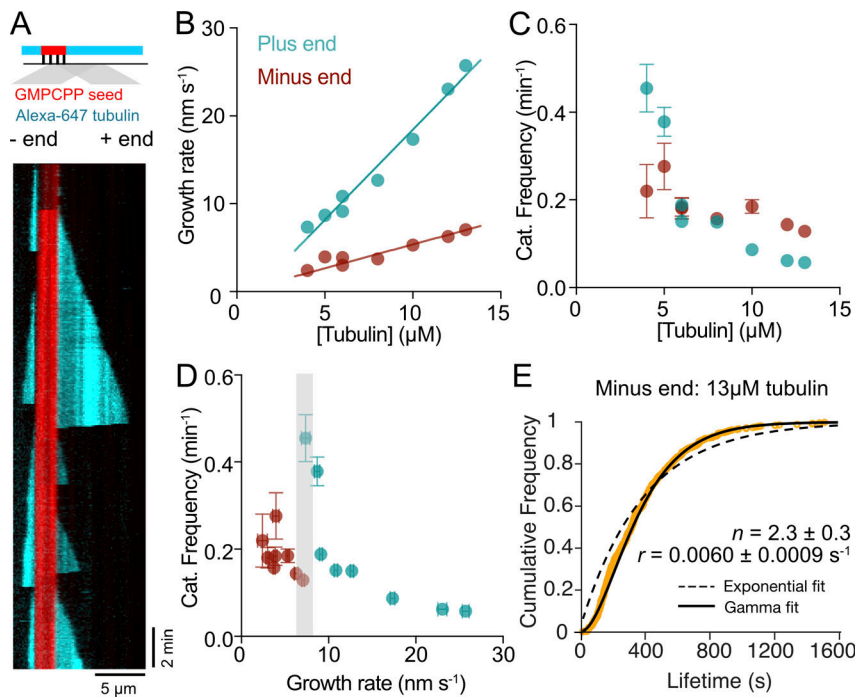
Strothman et al.
Mechanisms of microtubule minus-end catastrophe

Journal of Cell Biology
https://doi.org/10.1083/jcb.201905019

2842

Figure 1. **Minus ends have distinct dynamics and undergo aging during growth. (A)** Top: Schematic showing experimental set-up. Bottom: Representative kymograph showing characteristic differences between the two microtubule ends (8 µM tubulin). **(B)** Microtubule growth rates as a function of tubulin concentration. Error bars represent the SE of each independent experiment per condition (n = 13–285). Any error bars that are not visible are smaller than the size of the data point. **(C)** Microtubule frequency of catastrophe (Cat.) as a function of tubulin concentration. Error bars represent counting error (n = 13–241). **(D)** Microtubule frequency of catastrophe re-plotted as a function of corresponding growth rate; data are from panels B and C. The shaded area indicates matching growth rates of plus and minus ends. **(E)** Cumulative distribution of lifetimes of minus ends (13 µM tubulin). Lifetimes were pooled from two independent experiments (n = 417). The dashed line represents exponential fit, and the solid line represents gamma fit. n and r parameters represent gamma distribution step and rate parameters, respectively. See Materials and methods for experimental details.

tubulin concentration, correlating with the increase in microtubule growth rate (Bieling et al., 2007). Additionally, increase in growth rate (achieved by increasing tubulin concentration) is typically accompanied by suppression of catastrophe frequency (Walker et al., 1988; Drechsel et al., 1992; Gardner et al., 2011b), presumably due to the larger size of the stabilizing nucleotide cap (Duellberg et al., 2016; Rickman et al., 2017). We thus wondered whether the enhanced stability of microtubule minus ends is a result of inherently larger stabilizing nucleotide caps at minus ends.

To compare the size of the GTP cap at plus and minus ends, we analyzed localization of EB1-GFP at growing microtubule ends (Fig. 2 A). A direct comparison of EB1 comets at ends of microtubules grown with 40 µM tubulin revealed that slower-growing minus ends have, on average, shorter EB1-comet decay lengths (minus end: 272 ± 10 nm [95% CI; n ≥ 865 linescans]; plus end: 383 ± 20 nm [95% CI; n ≥ 587 linescans]; Fig. 2 B, closed circles). To investigate whether the growth rate alone sets the size of the EB1 comets at both ends, we then used 20 µM tubulin to obtain slow plus-end growth rates to match those measured at the minus ends at 40 µM tubulin (Fig. 2 B, open circles). We found that in 20 µM tubulin plus ends grew at the same rate (35 ± 3 nm s^{-1}, SE, n = 59) as minus ends in 40 µM tubulin (34 ± 5 nm s^{-1}, SE, n = 29) and that the corresponding average comet lengths were matched in these conditions (plus end at 20 µM tubulin: 276 ± 28 nm [95% CI; n ≥ 1220 linescans]; minus end at 40 µM tubulin: 272 ± 10 nm [95% CI; n ≥ 865 linescans]). Our results demonstrate that average EB1-comet size is set by the average growth rate, irrespective of the microtubule end. Importantly, even in the presence of EB1, minus ends exhibited lower frequency of catastrophe as a function of growth rate than plus ends, over a range of tubulin concentrations (Fig. S2 A). In other words, when plus and minus ends are growing at the same

growth rates (in different tubulin concentrations), their cap sizes are equivalent; yet, minus ends have longer lifetimes. We thus conclude that the average size of EB1 comets alone does not define microtubule lifetime.

To measure minus-end cap size in the absence of EB1, we performed tubulin dilution experiments. Here, we grew dynamic microtubules in the presence of 6, 12, or 18 µM tubulin in a microfluidic device and, while imaging, rapidly exchanged solutions to wash out soluble tubulin with sub-second resolution (Fig. S2 B). Consistent with previous reports (Voter et al., 1991; Walker et al., 1991; Duellberg et al., 2016; Ti et al., 2016), we observed a characteristic delay between tubulin washout and the onset of microtubule catastrophe, which we interpreted as the time during which the stabilizing cap is lost. We found that, in all investigated conditions, minus ends displayed shorter average delay times than plus ends (average across conditions: minus end: 4.7 ± 0.3 s, SE, n = 160; plus end: 8.6 ± 0.3 s, SE, n = 271; Fig. 2, C and D). Delay times increased with instantaneous growth rate determined before dilution (Fig. S2 C), consistent with the idea that faster growth rates result in larger stabilizing caps. Similar to a recent finding for microtubule plus ends (Duellberg et al., 2016), we observed slight depolymerization of both microtubule ends during the delay period, distinct from the fast microtubule depolymerization that follows catastrophe. We found that the shrinkage length before catastrophe scaled with the average growth rate before washout, with minus-end shrinkage lengths smaller than those observed at plus ends (Fig. S2 D). Based on these results, we conclude that growing minus ends have smaller stabilizing nucleotide caps than plus ends, corresponding to their slower growth rates. Therefore, the increased stability of minus ends cannot be explained by the relative size of their stabilizing caps.
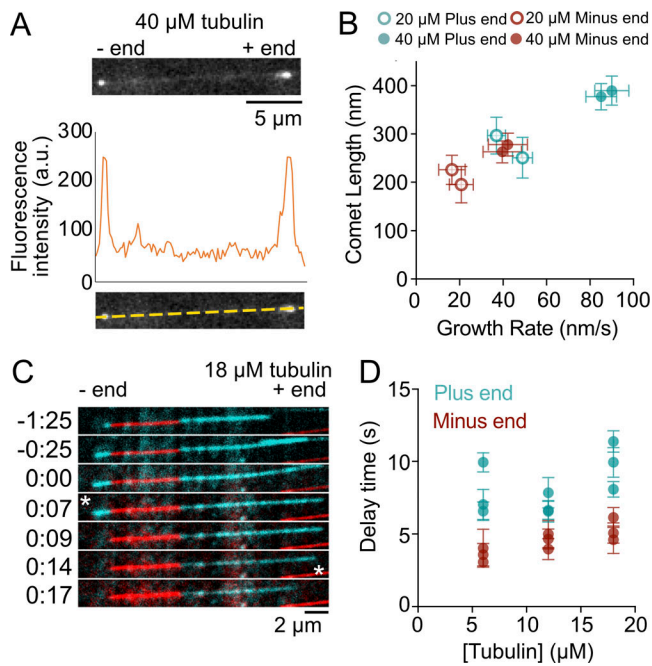
Figure 2. Minus-end cap size is small and scales with growth rate. **(A)** Representative image of EB1-GFP at both growing ends of a single microtubule (40 µM tubulin). A linescan was drawn along this microtubule to generate intensity values along the microtubule, showing two distinct peaks at either end. **(B)** Average EB1-comet length as a function of average growth rate of plus and minus ends in 20 or 40 µM tubulin with 200 nM EB1-GFP. Two independent repeats were done for each condition. Comet-length error bars are 95% CI from the fit. Growth rate is weighted average of individual growth events, and error is weighted SD. Weights are determined as the inverse of 95% CI of the linear fit to individual growth events. **(C)** Representative time lapse of a microtubule pre-grown with 18 µM tubulin undergoing tubulin washout. 0:00 time point indicates time of washout; asterisks indicate time of catastrophe for each end (minutes:seconds). **(D)** Mean delay times for each end are shown from three independent repeats of each tubulin concentration.

GMPCPP-tubulin off-rate at minus ends is significantly lower than that at plus ends

While our results showed that the size of the GTP cap alone is not the determinant of minus-end lifetime, we wondered whether any potential differences in the off-rate of GTP-tubulin incorporated into growing microtubule ends may play a significant role in setting the microtubule catastrophe frequency (Bowne-Anderson et al., 2013). Based on a classic model of biological polymers (Oosawa, 1970), the first order GTP-tubulin off-rate (k^T_{off}) can be determined from the y-intercept of the linear regression for microtubule growth rate as a function of tubulin concentration (Fig. 1 B). Notably, in this representation, the k^T_{off} is so small that it has essentially no effect on the microtubule growth rate at tubulin concentrations needed for robust microtubule elongation and can therefore not be precisely determined (Gardner et al., 2011a).

An alternative approach to determine the k^T_{off} is to measure the depolymerization rate of microtubules grown with GMPCPP, a slowly hydrolysable GTP analogue (Hyman et al., 1992). The GMPCPP microtubule lattice structure was recently validated as a faithful structural mimic of GTP-microtubule lattice (Zhang

et al., 2018); however, a direct comparison of GMPCPP-microtubule plus- and minus-end depolymerization rates has not been reported previously. To measure the GMPCPP-microtubule depolymerization rate at both ends, we polarity-marked microtubules with Cy5-labeled GMPCPP-tubulin, so that faster-growing plus ends had larger stretches of Cy5-tubulin (Fig. 3 A; see Materials and methods). By observing GMPCPP-microtubule depolymerization over 15 h, we determined that the minus end had a significantly lower tubulin off-rate of 0.054 ± 0.004 s⁻¹ (SE, n = 56) when compared with the plus-end off-rate of 0.144 ± 0.006 s⁻¹ (SE, n = 72; Fig. 3 B). Given this significant difference in the tubulin off-rate at the two ends, we hypothesize that although the absolute size of the GTP cap is smaller, the minus-end GTP cap may be more stable. Thus, we conclude that the difference in the tubulin off-rate may be the primary determinant of minus-end lifetime.

Kinesin-14 HSET suppresses minus-end tubulin-off rate, in contrast to kinesin-13 MCAK

Based on our findings, we expect that modulation of the GTP-tubulin off-rate would have a specific effect on catastrophe frequency without significantly affecting the mean growth rate (Bowne-Anderson et al., 2013; see Materials and methods). To test this hypothesis, we used two human mitotic kinesin motor proteins, MCAK and HSET. MCAK is a kinesin-13 motor well known for its function as a microtubule depolymerase. MCAK has been shown to robustly depolymerize GMPCPP-stabilized microtubules in vitro, directly increasing the tubulin off-rate at both microtubule ends (Desai et al., 1999; Hunter et al., 2003; Helenius et al., 2006). Consistent with previous reports, we found that the addition of 10 nM MCAK resulted in rapid depolymerization of GMPCPP-microtubules at both plus (7.7± 0.2 nm s⁻¹, SE, n = 139) and minus (8.0 ± 0.3 nm s⁻¹, SE, n = 140) ends (Fig. 3, C and D). HSET is a member of the kinesin-14 family of minus-end–directed motors. While HSET's effect on microtubule dynamics has not previously been reported, Kar3, a *Saccharomyces cerevisiae* member of the kinesin-14 family, was previously shown to act as a microtubule depolymerase (Sproul et al., 2005). We thus wondered whether the *Homo sapiens* kinesin-14 HSET might also modulate the GTP-tubulin off-rate at microtubule ends.

When added to GMPCPP-stabilized microtubules, HSET molecules diffused along the microtubule lattice and accumulated at minus ends over time, consistent with previous reports using the *Drosophila melanogaster* HSET homologue Ncd (Fink et al., 2009). However, in the presence of HSET, we did not observe any discernible depolymerization at either microtubule end over the course of a 15-min-long movie, similar to the control (Fig. 3 C). It has recently been shown that the presence of soluble tubulin induces robust minus-end–directed processivity of HSET molecules (Norris et al., 2018). We thus tested whether the addition of soluble tubulin to HSET changed its ability to depolymerize microtubules, and again, we observed no depolymerization (Fig. S3, A and B). However, when we combined 10 nM GFP-HSET with 10 nM MCAK, we observed rapid depolymerization at microtubule plus ends only (Fig. 3 C). The addition of HSET to MCAK significantly decreased depolymerization at
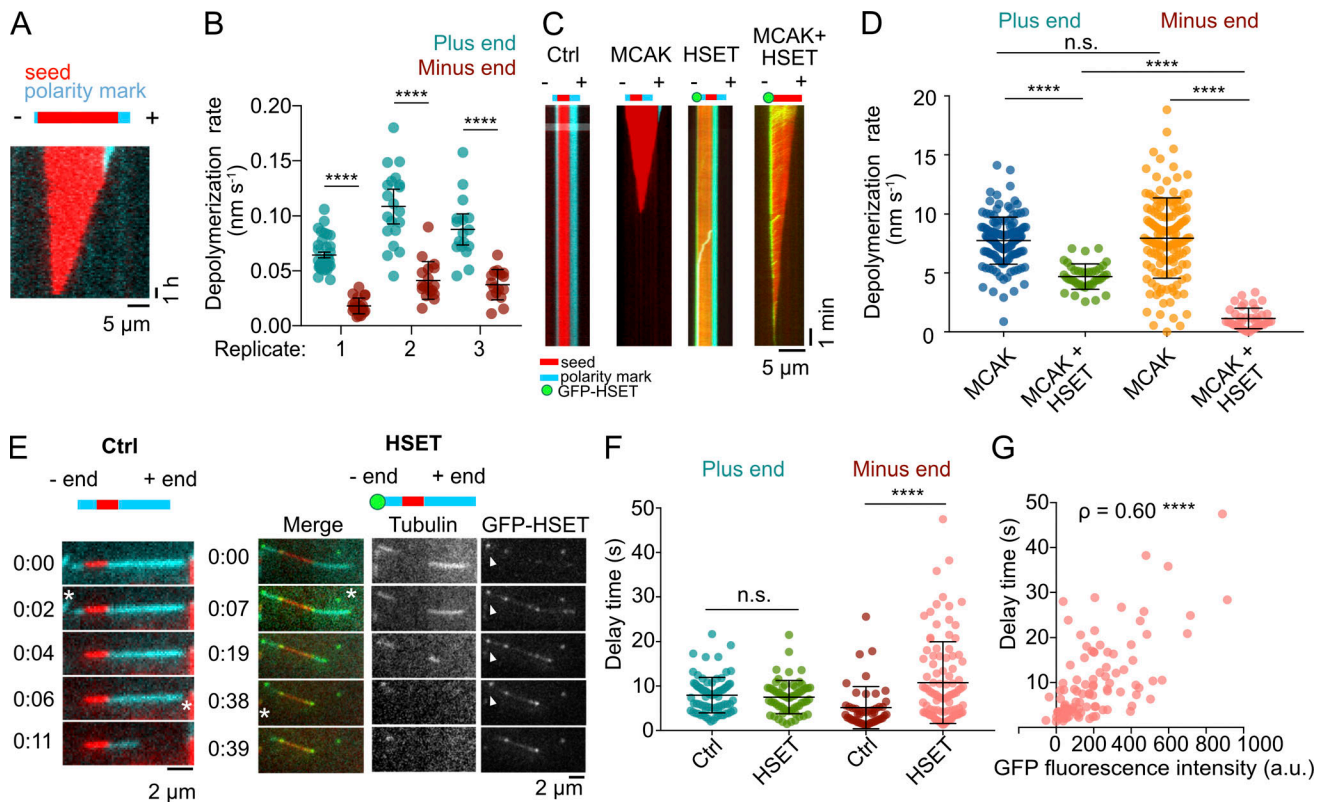
Figure 3. Minus ends have a lower tubulin off-rate, which is modulated by kinesins MCAK and HSET. (A) Representative kymograph of a polarity-marked GMPCPP-seed depolymerization experiment. The plus and minus ends are denoted on the kymograph. **(B)** Depolymerization rates of polarity marked GMPCPP microtubules from three independent experiments. Mean and SE are plotted for each group ($n \geq 16$). ****, $P \leq 0.0001$ using unpaired Welch's t tests. **(C)** Representative kymographs of GMPCPP seeds in different conditions: control (Ctrl), +10 nM GFP-HSET, +10 nM MCAK, or +both 10 nM GFP-HSET and 10 nM MCAK. Seeds are polarity marked with Alexa Fluor 647 tubulin in control, HSET, and MCAK conditions, but not with both motors. **(D)** GMPCPP-microtubule depolymerization rates of MCAK, and MCAK+HSET conditions at the plus and minus end. In the MCAK-alone condition, plus and minus ends are differentiated by the polarity mark. In the double-motor condition, the ends are differentiated by HSET localization. Data represent two independent repeats of each condition. Plus end: MCAK (blue), $n = 139$; MCAK + HSET (green), $n = 40$; minus end: MCAK (gold), $n = 140$; MCAK + HSET (pink), $n = 40$. Mann-Whitney U tests were performed for plus- and minus-end conditions separately. ****, $P \leq 0.0001$. **(E)** Representative time lapses of dilution experiments in the absence or presence of 100 nM HSET. Asterisks mark time of catastrophe at either end. Arrowheads in HSET condition indicates GFP-HSET tip localization. The time stamp indicates time after washout (min:s). **(F)** Delay times per end in the absence or presence of 100 nM HSET. $n = 3$ independent repeats for the control, and $n = 4$ independent repeats for +HSET condition. **(G)** Minus end with HSET delay times as a function of GFP fluorescence intensity (background subtracted; see Materials and methods). $n = 97$ delay times from four independent repeats. Spearman's rho test = 0.060; ****, $P \leq 0.0001$.

minus ends, inducing a sevenfold reduction in the minus-end depolymerization rate when compared with the MCAK-alone condition (Fig. 3 D). In contrast, HSET only mildly suppressed the plus-end depolymerization rate (1.7-fold), possibly due to the residual localization of HSET all along the microtubule lattice. We conclude that HSET antagonizes the MCAK-induced increase in the tubulin off-rate at microtubule minus ends.

To further investigate whether HSET directly suppresses tubulin off-rate, we repeated tubulin dilution experiments using microtubules grown with 12 µM tubulin in the presence or absence of 100 nM GFP-HSET during both the growth and washout phases (Fig. 3 E). We found that HSET had no significant effect on plus-end delay times; however, we observed a significant increase in minus-end delay times in the presence of HSET (Fig. 3 F). Individual delay times correlated with the average GFP-HSET fluorescence intensity at the microtubule tip following tubulin washout (Fig. 3 G), indicating that HSET directly stabilized minus ends after washout, consistent with suppressing

the GTP cap removal. We thus conclude that, in contrast to MCAK, HSET directly suppresses the tubulin off-rate at microtubule minus ends.

HSET suppresses minus-end catastrophe and protects minus ends against MCAK

Based on our finding that HSET suppresses tubulin off-rate, we predicted that HSET would suppress catastrophe frequency, in contrast to the well-known catastrophe-promoting activity of MCAK (Desai et al., 1999; Newton et al., 2004; Gardner et al., 2011b). To test this hypothesis, we grew dynamic microtubules with 10 µM tubulin and 10 nM GFP-HSET. In these conditions, HSET walked processively toward the minus end, where it tip-tracked the growing minus end (Fig. 4 A). Microtubule growth and shrinkage rates at both the plus and minus ends were not significantly different in the presence or absence of HSET (Fig. 4 B and Fig. S3 C). HSET did not significantly affect plus-end catastrophe, but strongly and specifically suppressed minus-end
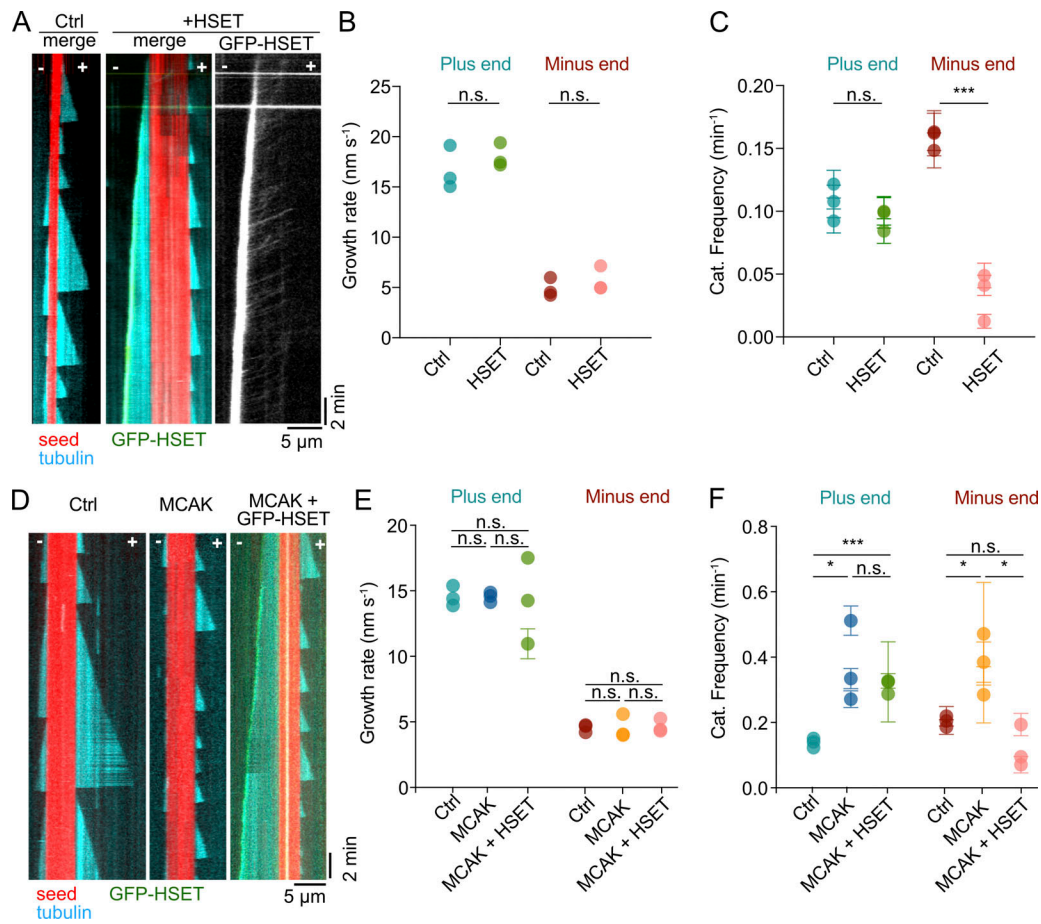
Figure 4.   **HSET suppresses minus-end catastrophe and protects minus ends against MCAK. (A)** Representative kymographs from movies comparing dynamics of microtubules grown in 10 µM tubulin with and without 10 nM GFP-HSET. *n* = 3 independent repeats per condition. Plus-end control: *n* = 176, 258, 123; plus-end HSET: *n* = 235, 276, 157. Minus-end control: *n* = 93, 97, 24; minus-end HSET: *n* = 88, 120, 59. Error bars are SEM. **(C)** Catastrophe frequency of plus and minus ends. Plus-end control: *n* = 155, 232, 121; plus-end HSET: *n* = 224, 242, 153. Minus-end control: *n* = 85, 92, 23; minus-end HSET: *n* = 67, 37, 13. Error bars represent counting error. **(D)** Representative kymographs of microtubules grown in 10 µM tubulin, 10 µM tubulin with 10 nM MCAK, and 10 µM tubulin with 10 nM of both MCAK and GFP-HSET. **(E)** Average growth rates of dynamic plus and minus ends in a control, with MCAK, and with both MCAK + HSET. Plus-end control: *n* = 88, 200, 79; plus-end MCAK: *n* = 132, 132, 125; plus-end MCAK + HSET: *n* = 235, 8, 249. Minus-end control: *n* = 74, 118, 56; minus-end MCAK: *n* = 12, 9, 41; minus-end MCAK + HSET: *n* = 29, 13, 34. **(F)** Catastrophe frequency of plus and minus ends in a control, with MCAK, and with both MCAK and HSET. Plus-end control: *n* = 66, 154, 63; plus-end MCAK: *n* = 113, 129, 118; plus-end MCAK + HSET: *n* = 216, 7, 220. Minus-end control: *n* = 67, 109, 54; minus-end MCAK: *n* = 11, 9, 39; minus-end MCAK + HSET: *n* = 24, 8, 32. Error bars represent counting error. Multiple unpaired *t* tests were performed for all plus- and minus-end conditions. n.s., P ≥ 0.05; *, P ≤ 0.05; ***, P ≤ 0.001.

catastrophe (Fig. 4 C). In contrast, MCAK significantly increased catastrophe at both plus and minus ends (Fig. 4, D and F) without affecting the growth rate at either end (Fig. 4 E), consistent with previous reports at the plus end alone (Montenegro Gouveia et al., 2010; Gardner et al., 2011b). When HSET and MCAK were combined, we observed significant suppression of catastrophe, specifically at the minus end (Fig. 4, D and F). These findings directly correlate the effects of each of the motors on the GTP-tubulin off-rate with their specific and antagonistic modulation of microtubule catastrophe.

Conclusions

Classic in vitro studies of microtubule dynamics have long established that, like plus ends, microtubule minus ends stochastically switch between periods of growth and shrinkage, albeit with distinct dynamic parameters (Walker et al., 1988). The

factors driving these differences remained unknown, keeping the minus end at the "dark side of microtubule dynamics" (Desai and Mitchison, 1997) for decades. Recent studies of microtubule minus-end binding proteins elucidated the importance of minus-end regulation in cells (Hendershott and Vale, 2014; Jiang et al., 2014, 2017; Yau et al., 2014; Noordstra et al., 2016; Atherton et al., 2017). In this study, we used in vitro reconstitution of microtubule dynamics to reexamine the inherent mechanisms of minus-end catastrophe.

Microtubule catastrophe occurs via the loss of a protective cap of GTP-tubulin, the size of which is widely considered to be the determinant of microtubule plus-end stability. When microtubule growth rate is increased in vitro by increasing tubulin concentrations, the plus-end EB-comet size also increases (Bieling et al., 2007), while microtubule catastrophe is suppressed (Walker et al., 1988; Drechsel et al., 1992; Gardner et al.,

2011b). Furthermore, larger EB comets have been directly correlated with prolonged stability against dilution-induced catastrophe at microtubule plus ends (Duellberg et al., 2016). The size of the GTP cap is set by the difference between the microtubule growth and GTP hydrolysis rates (see Materials and methods); thus, modulation of the GTP hydrolysis rate may be a potent mechanism for setting the GTP cap size, and consequently regulating microtubule stability. Indeed, a recent study linked smaller EB comets, presumably due to a faster GTP hydrolysis rate, to increased dynamicity of *Caenorhabditis elegans* tubulin (Chaaban et al., 2018), and modulation of the GTP hydrolysis rate has been implicated in regulation of microtubule plus-end catastrophe by several microtubule-associated proteins (Maurer et al., 2014; Zhang et al., 2017, 2018). Structural studies have proposed a mechanism of tubulin conformational changes during hydrolysis at the plus end (Nogales et al., 1998, 1999; Alushin et al., 2014); however, it is not clear whether the minus end may have a differing mechanism or rate of GTP hydrolysis. Our results show a universal scaling between the EB1-comet size and the growth rate at both ends, suggesting that the overall rate of GTP hydrolysis at the minus end is unlikely to be different from that at the plus end. Moreover, our finding that minus ends display the same lifetimes as plus ends with significantly smaller EB comets implies that the absolute size of the GTP cap is not the primary determinant of microtubule lifetime.

How can minus ends maintain their stability in spite of their small GTP caps? While our results show that an increase in minus-end growth rates also correlates with larger EB comets and enhanced stability, the sensitivity of minus ends to the GTP cap size appears to be much lower than that of the plus ends. We do not think that potential differences in rates of GDP-tubulin dissociation at the two ends following catastrophe underlie this distinct sensitivity; we found rapid minus-end depolymerization rates to be no slower than those at plus ends upon catastrophe (Fig. S3 C). Instead, based on our results, we propose that this difference is due to the significantly lower rate of GTP-tubulin dissociation at dynamic minus ends. Given that even a couple of layers of unhydrolyzed tubulin are sufficient to prevent microtubule catastrophe (Drechsel and Kirschner, 1994; Caplow and Shanks, 1996), we conclude that the small, but stable, GTP-tubulin cap may be the key to minus-end longevity.

Beyond the simple models using kinetic rates of tubulin association, dissociation, and GTP hydrolysis, it is increasingly clear that the interplay of kinetics and microtubule end structure ultimately encodes microtubule end stability (Brouhard and Rice, 2018). Dynamic remodeling of end structure over the period of microtubule growth has been implicated in microtubule aging, providing a potential explanation for the observed non-single-step kinetics of plus-end catastrophe (Coombes et al., 2013). Our measured distributions of minus-end lifetimes show that minus-end catastrophe cannot be modeled as a single-step random process, implying that, like plus ends, minus ends undergo an aging process. Consistent with this finding, a recent cryo-electron tomography investigation of the microtubule end structures reported no statistically significant differences between the two ends (Atherton et al., 2018). Importantly, this study did not control for the age of the microtubules. Future

high-resolution studies are needed to detect potential signatures of structural aging over the microtubule lifetime at either end. Structural effects on microtubule end dynamics may well be encoded in the microtubule lattice; an intense area of recent study (Geyer et al., 2015; Aumeier et al., 2016; von Loeffelholz et al., 2017; Vemu et al., 2018). Notably, minus ends display higher frequency of microtubule rescue (transition from shrinking to growing state), and newly generated minus ends may be stable against depolymerization both in vitro and in cells (Walker et al., 1989; Tran et al., 1997; Goodwin and Vale, 2010; Tanaka et al., 2012; Hendershott and Vale, 2014; Jiang et al., 2014). The mechanisms of microtubule rescue and its regulation remain a mystery and more work is needed to understand whether and how microtubule lattice structure encodes rescue at either end (Gardner et al., 2013; Fees and Moore, 2019; Kuo et al., 2019; Lawrence and Zanic, 2019).

A number of kinesin motors have been identified as regulators of microtubule dynamics; our results now add human kinesin-14 HSET to this list. Unlike kinesin-13 MCAK, which does not discriminate between the two ends, HSET's regulatory activity is restricted to the minus end, since its directionality strongly enhances its localization to minus-end tips. Both MCAK and HSET have a specific effect on microtubule catastrophe, without changing the microtubule growth or shrinkage rates (Newton et al., 2004; Montenegro Gouveia et al., 2010), consistent with the idea that they are regulating GTP-tubulin off rate, which is predicted to primarily affect catastrophe, and not growth or shrinkage. Specific regulation of minus-end catastrophe by HSET is in stark contrast with the effects of other known minus-end regulators. For example, proteins from the CAMSAP family of minus-end regulators exert simultaneous effects on several dynamic parameters: while they suppress catastrophe, they also slow down minus-end growth, suggesting a distinct mechanism from that of HSET (Hendershott and Vale, 2014; Jiang et al., 2014).

Overall, our finding that MCAK and HSET target the same kinetic rate, but regulate it antagonistically, suggests a general mechanism for specific regulation of microtubule catastrophe. We do not know whether HSET sterically inhibits localization of MCAK to minus ends, as reported for CAMSAP (Atherton et al., 2017); nevertheless, our results demonstrate an intriguing phenomenon where HSET effectively converts MCAK into a plus-end–specific depolymerase. MCAK and HSET are both mitotically active kinesins, and perturbations of either result in large-scale disruptions in spindle length and morphology (Ohi et al., 2007; Cai et al., 2009; Domnitz et al., 2012). Though HSET has previously been shown to be a force balance factor in the spindle (Mountain et al., 1999; Cai et al., 2009; Hentrich and Surrey, 2010; Reinemann et al., 2018), as well as a kinesin involved in pole focusing and spindle organization (Cai et al., 2009; Hepperla et al., 2014), its role in regulating minus-end dynamics within the spindle, and potentially counterbalancing MCAK, has not yet been studied. We hope that our study will inspire development of more refined, holistic models encompassing the dynamics of both microtubule ends, and lead to future studies in cells, uncovering how regulation of both microtubule ends is integrated to give rise to the dynamic cellular microtubule architecture.

Materials and methods
Protein biochemistry
Tubulin and microtubule preparation
Tubulin was purified from porcine and bovine brains using standard protocols (Castoldi and Popov, 2003; Gell et al., 2011). Briefly, porcine tubulin was purified by cycles of polymerization/depolymerization followed by purification on a phosphocellulose column and a final subsequent polymerization/depolymerization cycle (Gell et al., 2011). Bovine tubulin was purified by cycles of polymerization/depolymerization using the high-molarity Pipes buffer method (Castoldi and Popov, 2003). Labeling of tubulin with TMR (tetramethylrhodamine), Alexa Fluor 488, Cy5, and Alexa Fluor 647 dyes (Invitrogen) was performed as previously described (Hyman et al., 1991). GMPCPP-stabilized microtubule seeds were prepared as previously described (Gell et al., 2010) by polymerizing a 1:3 molar ratio of TMR-labeled/unlabeled tubulin in the presence of GMPCPP at 37°C for 1 h, before being diluted and spun down at 20 pounds per square inch (126,000 × g) for 5 min. Concentrated seeds were then re-suspended in 100 µl BRB80 (80 mM Pipes/KOH, pH 6.8, 1 mM MgCl$_2$, and 1 mM EGTA) and diluted 5–20 times for use in experiments.

Other proteins
EB1–GFP was expressed in *Escherichia coli* and purified as previously described (Zanic et al., 2009). His6-HSET tagged with enhanced GFP was expressed in *Spodoptera frugiperda* (Sf9 cells) and purified as previously described (Norris et al., 2018). Human MCAK-His6 was expressed in Sf9 cells and purified as previously described (Helenius et al., 2006).

Assay conditions and imaging
Chamber preparation
Microscope chambers were constructed with 18 × 18-mm and 22 × 22-mm coverslips separated by parafilm, briefly melted to create channels 0.1 mm thick, 2–3 mm wide, and 18 mm long. Glass coverslips (no. 1.5; Corning) were cleaned in piranha solution (3:7 H$_2$O$_2$/H$_2$SO$_4$ by volume) before silanization with a 0.05% solution of dichlorodimethylsilane in trichloroethylene, as previously described (Gell et al., 2010). To immobilize microtubules, channels were incubated with 1:50 anti-TMR antibody (Life Tech.) in BRB80 for 5 min and incubated with 1% pluronic F127 in BRB80 for 30 min, and, finally, diluted GMPCPP seeds in BRB80 were washed in and immediately washed out. Rinses between steps were done with BRB80.

Microfluidic devices
Y-shaped microfluidic devices were prepared similarly to those previously described by Duellberg et al. (2016), but with two branched inlets instead of three. Silicon molds with negative channel patterns were produced using deep reactive ion etching. A mixture of polydimethylsiloxane (PDMS) and curing agent (Dow Corning; 10:1 wt/wt) was poured over a mold, degassed for 20 min at room temperature, and polymerized for 4 h at 60°C. Holes for the inlet and outlet channels were created in the peeled-off PDMS block using biopsy punchers (Miltex; diameter 1.5 mm). The structured side of the PDMS and a 22 × 22-mm

glass coverslip were treated with air plasma (PDC-32G; Harrick Plasma) for 20 s. A small area of 4 × 10 mm, where imaging was to occur, was protected from plasma radiation by a small PDMS block to ensure the integrity of the surface functionalization. Immediately after plasma treatment, the exposed sides were bonded to form the channels, and tubing (Tygon; inner diameter of 0.5 mm) was connected to the PDMS inlets/outlet and Hamilton gas tight syringes (1,000 ml total volume; used for channel preparation only). The microfluidic devices were used for TIRF microscopy experiments immediately after assembly.

Imaging
Imaging was performed as previously described (Lawrence et al., 2018) using a Nikon Eclipse Ti microscope with a 100×/1.49 NA TIRF objective and Andor iXon Ultra EM-CCD (electron-multiplying charge-coupled device) and NEO sCMOS (scientific complementary metal-oxide semiconductor) cameras; 488-nm, 561-nm, and 640-nm solid-state lasers (Nikon Lu-NA); Finger Lakes Instruments HS-625 high-speed emission filter wheel; and standard filter sets. An objective heater was used to maintain the sample at 35°C. Images were acquired using NIS-Elements (Nikon).

Microtubule dynamics assay
Dynamic microtubule extensions were polymerized from surface-bound GMPCPP-stabilized seeds as described previously (Gell et al., 2010). Imaging reactions consisted of BRB80 supplemented with 1 mM GTP (unless otherwise indicated) and anti-fade solution: 40 mM D-glucose, 40 µg/ml glucose oxidase, 16 µg/ml catalase, 0.08 mg/ml casein, 10 mM dithiothreitol, and 50 mM KCl. Protein concentrations used are indicated in the text. Fluorescently labeled tubulin was typically used at a ratio of between 5% and 10% of the total tubulin. Reactions containing HSET and/or MCAK were additionally supplemented with 1 mM ATP. Dynamics assays with HSET and/or MCAK were performed in the same way. MCAK was stored and diluted in BRB20 (20 mM Pipes/KOH, pH 6.8, 1 mM MgCl$_2$, and 1 mM EGTA), and control experiments contained an equivalent volume of BRB20 to MCAK conditions. GFP-HSET was diluted in BRB80, and control conditions contained an equivalent volume of HSET storage buffer (10 mM K-HEPES, pH 7.7, 300 mM KCl, 1 mM dithiothreitol, 100 µM MgCl$_2$, 100 µM ATP, and 20% sucrose). Dynamics experiments with motors used 10 µM tubulin, 7% labeled with Alexa Fluor 647 dye. Dynamics movies for the tubulin titration series and for dynamics with motors were imaged for 30 min at 0.2 frame per second (FPS), with the exception of the HSET-alone dynamics series. For this, the representative kymographs come from movies imaged at 0.2 FPS for 30 min, but careful measurements of growth rate, shrinkage rate, and catastrophe frequency for this series come from movies taken at 1 FPS for 30 min. For cumulative distribution function (CDF) analysis, dynamic experiments were repeated as above, using slightly different imaging conditions to detect small microtubule lifetime events. Dynamic microtubules grown with 6 µM or 13 µM tubulin were imaged for 1 h at 0.3 FPS, using an Optovar increased magnification (1.5×) to achieve a pixel size of 106 nm. Imaging was delayed for 10 min to allow the chamber to reach

steady state. For microtubule dynamics assay with EB1 comets, conditions were the same as described above with the following exceptions: 17 mM KCl and 0.01% methylcellulose were used in the imaging reaction. Images were taken at 0.5 FPS. All of the dynamics experiments were imaged using the EM-CCD camera.

Dilution experiments

Fast solution exchange in the micro-channel was achieved by switching the flow from two different inlets that were controlled by independent pumps (OB1 MK3; ElveFlow) and flow sensors (MFS2 and MFS3; ElveFlow) between pumps and inlets. To assemble a sample, short GMPCPP-stabilized, TMR-labeled microtubule seeds were introduced through one inlet and allowed to attach to the functionalized glass surface. To initiate microtubule growth, 6, 12, or 18 µM 20% Alexa Fluor 647–labeled tubulin was introduced through the first inlet at a constantly maintained flow rate of 7 µl/min for 90 s, and then flow was stopped for the remaining growth period. Imaging buffer was supplemented with 0.05% methylcellulose. After a short period of growth (5–10 min), sub-second tubulin washout was induced using a 50 µl/min flow of a washout reaction containing BRB80 and anti-fade, unchanged from the initial growth reaction besides tubulin. Plus and minus ends were differentiated by average growth rates before washout. Imaging during the growth phase was performed at 0.2 FPS and imaging of the 640-nm channel just before, during, and after washout was performed at 10 FPS for tubulin-only conditions using the CMOS camera (70-nm pixel). Dilution experiments containing HSET had 100 nM GFP-HSET present in both the growth and washout phases, supplemented with 100 nM unlabeled tubulin during the washout. Experiments comparing the effect of HSET were done at 6.7 FPS (640- and 488-nm channels) using the EM-CCD camera (160-nm pixel).

GMPCPP seed depolymerization

GMPCPP depolymerization experiments were done by growing TMR-labeled seeds as described above. Polarity marking was performed by incubating the coverslip-attached GMPCPP seeds with 0.5 µM 7% Cy5-labeled bovine tubulin with 1 mM GMPCPP in the imaging buffer (without GTP) for 15 min. All tubulin was then washed out with BRB80/anti-fade solution (without GTP), and the chambers were sealed with valap (33% wt/wt Vaseline, lanolin, and paraffin wax). Images were taken every 10 min for 15 h on the EM-CCD camera.

GMPCPP seed depolymerization with MCAK + HSET

GMPCPP seed depolymerization assays were performed similarly to the above. TMR-labeled seeds were prepared and bound to the chamber coverglass. Polarity marking was used in control, HSET, and MCAK conditions: 0.5 µM 7% Alexa Fluor 647 tubulin with 1 mM GMPCPP was flown into the chamber and let polymerize for 15 min before the experiment. After 15 min, this mixture was washed out and replaced with imaging buffer containing BRB80, 10 nM GFP-HSET, 10 nM MCAK, or both motors in a reaction mix with anti-fade lacking guanosine nucleotides, but supplemented with 1 mM ATP. Soluble tubulin was not present in the reaction mix unless indicated. To test the

effect of tubulin activation, the HSET condition was repeated in the absence of polarity marking, but in the presence of 100 nM 7% Alexa Fluor 647 tubulin. Images were taken every 3 s for 15 min on the EM-CCD camera.

Image analysis and determination of rate parameters
Microtubule dynamics parameters and lifetime analysis
Microtubule dynamics were analyzed by creating kymographs of dynamic microtubules in FIJI (Schindelin et al., 2012) using a custom-made plug-in. Polarity of microtubules was determined by comparison of growth rates at each end of the microtubule: faster growing ends were categorized as plus ends, and slower ones were categorized as minus ends. Microtubule dynamics parameters were determined as previously described (Zanic, 2016). Briefly, growth rates were determined by calculating the difference in distance over time between the start and end of a growth event. Catastrophe frequency was determined as a ratio of the total number of catastrophes observed over the total time microtubules spent in growth for a given movie. Microtubule lifetimes were defined for individual growth events as the total time from the onset of microtubule growth until the onset of catastrophe. Only fully observable lifetime events with a clearly defined start and end were included in any lifetime analysis. Analysis of dynamics in the presence of HSET and/or MCAK was performed in the same way. Shrinkage rate was determined by calculating the difference in distance over time between the start and end of the shrinkage event. Cumulative distributions of lifetimes and fits to exponential and gamma distributions were performed as previously described (Gardner et al., 2011b; Zanic, 2016). Specifically, for each condition, all lifetimes were used as input, and the best fit gamma parameters were determined using the gamfit function in the MATLAB Statistics toolbox (MathWorks, Inc.), specified by the gamma probability density function

$$f(t|n,\ s) = \frac{t^{n-1}e^{-t/s}}{s^n \Gamma(n)}\quad,$$

where $\Gamma(n)$ is the gamma function, n is a "shape" (also known as "step") parameter, and s is a "scale" parameter. The function gamfit returns maximum likelihood estimates and CIs for the shape and scale parameters. The reported rate parameter r was determined as the inverse of the scale parameter, $r = 1/s$, and the error was propagated from the CIs for the scale parameter.

Tubulin on- and off-rates

GTP-tubulin on- and off-rates were determined from measured growth rates as a function of tubulin concentration by linear regression analysis in MATLAB (MathWorks, Inc.), assuming

$$v_g = \frac{d}{13}\left(k_{on}[Tb] - k_{off}\right),$$

where $d = 8$ nm is the size of a tubulin dimer, k_{on} is the second order GTP-tubulin on-rate constant, and k_{off} is the first order GTP-tubulin off-rate constant. Given the relatively small values and large uncertainties in the y-intercept, this method is deemed not reliable for precise determination of the GTP-tubulin off-rate. For this reason, k_{off} was additionally determined from the

depolymerization rate of GMPCPP microtubules, assuming a 14-protofilament microtubule structure, as previously described (Hyman et al., 1992). GMPCPP microtubule depolymerization rates were calculated by placing points at the beginning and end of each shrinkage event and categorized as plus or minus end based on polarity marking. When polarity marks were absent (i.e., in the presence of GFP-HSET), HSET minus-end directionality and localization were used to differentiate the microtubule ends. Outliers were removed using the ROUT method (robust regression and outlier removal; GraphPad Prism), with Q = 0.1%.

EB1-comet length

Image analysis was performed by generating kymographs of microtubule growth events. For each tubulin concentration, 20 microtubules for which both plus and minus ends could be analyzed were selected to determine catastrophe frequency, average growth rate, and average EB1-comet length. The characteristic decay length of the EB1 comets was determined using custom MATLAB functions. The microtubule tip location for each time frame was estimated by fitting a line through two manually clicked points at the beginning and end of a growth event on each kymograph. The pixel with the brightest EB1 intensity within ±5 pixels of the estimated tip location was determined for each time frame and assigned as the bona fide microtubule tip location. Average tip intensity (I^{tip}) and its SD (σ^{tip}) of a given growth event were calculated, and any time frames with tip intensity lower than $I^{tip} - \sigma^{tip}$ were excluded. The remaining points were used to fit a linear function to approximate the growth rate. Time frames with fit residuals more than one SD away from the mean residuals were excluded. The remaining points were used to fit a linear function to determine the growth rate of the given event. For each time frame within the given growth event, the microtubule tips were aligned, and an average intensity profile was calculated. The lattice intensity was determined by averaging the intensity values between 20 and 25 pixels away from the tip. This average lattice intensity was subtracted from intensity profiles from each remaining time frame. Manual inspection was performed to remove any growth events in which the tip locations were not successfully determined by the above automated procedures. The remaining growth events were used to determine the average growth rate (v_g) and its SD (σ_{v_g}) weighted with inverse of the 95% CI of the fitting procedure. Individual growth events were further excluded if they were not within $v_g \pm \sigma_{v_g}$. Individual intensity profiles from each individual time frame from the remaining growth episodes were used to generate a super-averaged intensity profile. The super-averaged intensity profile in the range of 1 pixel in the solution background and 20 pixels along the microtubule lattice was fit to an exponential decay convolved with a Gaussian function, given by

$$\frac{A}{2}\left[e^{\left(\frac{\sigma^2}{2\lambda^2}-\frac{x-x_0}{\lambda}\right)}\right]\left[1+erf\left(\frac{x-x_0}{\sigma\sqrt{2}}-\frac{\sigma}{\lambda\sqrt{2}}\right)\right]+\frac{B}{2}\left[1+erf\left(\frac{x-x_0}{\sigma\sqrt{2}}\right)\right],$$

where A is the intensity value at the tip, B is the difference between average lattice intensity and solution background, σ is the

experimentally determined full width at half maximum of the point spread function, x_0 is the offset in the tip position due to convolution, and λ is the comet decay length.

Tubulin dilution image analysis

Delay times, shrinkage length, and instantaneous velocity before washout were determined as previously described (Duellberg et al., 2016), and outliers were removed using the ROUT method, with Q = 0.1%. For instantaneous growth rate, microtubules were grown for 5–10 min in 20 µM tubulin. Instantaneous growth rate was determined by imaging microtubules at 10 FPS for 8–10 s before washout, and measuring the average growth rate during this time. Representative dilution time lapse in Fig. 2 C was background-subtracted using an average rolling ball subtraction to visualize microtubule over time despite different background fluorescent intensities. Fluorescence intensity of GFP-HSET was determined by drawing a linescan over the kymograph of the microtubule tip following washout, and taking the mean intensity measurement. Background was subtracted by taking the mean intensity of a small rectangular area (3-pixel width × length of linescan) in the solution area adjacent to each microtubule tip, so that each individual event had its own background subtraction to account for uneven illumination in the TIRF field of view. Corresponding delay times were plotted as a function of GFP-HSET tip intensity during washout.

Comparison of our cap-size measurements with the predictions from the theoretical model of Bowne-Anderson et al. (2013)

A previously developed theoretical model of microtubule catastrophe using a coupled-random GTP hydrolysis mechanism found that, in the regimen of robust microtubule growth ($k_{off} \ll k_{on}[Tb]$), the microtubule catastrophe frequency as a function of tubulin concentration may be modeled by

$$f_{cat} \approx \frac{13}{n}\, k_{off}\, \frac{h}{h+k_{on}[Tb]}\,,$$

where n is the gamma distribution step parameter, h is the GTP-tubulin hydrolysis rate, and k_{on} and k_{off} are GTP-tubulin on- and off-rates, respectively (Bowne-Anderson et al., 2013). Using our experimentally determined tubulin on-rates (minus: 0.88 ± 0.04 µM^{-1} s^{-1}; plus: 3.34 ± 0.02 µM^{-1} s^{-1}) and off-rates (minus: 0.054 ± 0.004 s^{-1}; plus: 0.144 ± 0.006 s^{-1}) and assuming gamma step parameter n = 2 for both ends, the best fit of this theoretical model to our catastrophe frequency as a function of tubulin concentration data yields a hydrolysis rate h = 0.07 ± 0.02 s^{-1} (maximum likelihood estimate with 95% CI) for both ends. The steady-state GTP cap size λ can be modeled as $\lambda = v_g/h$, where GTP-tubulin subunits are added to the cap with the net polymerization rate v_g and removed through the process of GTP hydrolysis with rate h, which is assumed to be independent of tubulin concentration. Under these assumptions, the hydrolysis rate of 0.07 ± 0.02 s^{-1} would correspond to the GTP cap decay size of 290 ± 80 nm for microtubules growing at 20 nm/s, in excellent agreement with both our EB-comet decay length measurements (Fig. 2 B) and the shrinkage length before dilution measurements (Fig. S2 D).

References

Akhmanova, A., and C.C. Hoogenraad. 2015. Microtubule minus-end-targeting proteins. *Curr. Biol.* 25:R162–R171. https://doi.org/10.1016/j.cub.2014.12.027

Akhmanova, A., and M.O. Steinmetz. 2015. Control of microtubule organization and dynamics: two ends in the limelight. *Nat. Rev. Mol. Cell Biol.* 16:711–726. https://doi.org/10.1038/nrm4084

Alushin, G.M., G.C. Lander, E.H. Kellogg, R. Zhang, D. Baker, and E. Nogales. 2014. High-resolution microtubule structures reveal the structural transitions in αβ-tubulin upon GTP hydrolysis. *Cell.* 157:1117–1129. https://doi.org/10.1016/j.cell.2014.03.053

Atherton, J., K. Jiang, M.M. Stangier, Y. Luo, S. Hua, K. Houben, J.J.E. van Hooff, A.-P. Joseph, G. Scarabelli, B.J. Grant, et al. 2017. A structural model for microtubule minus-end recognition and protection by CAMSAP proteins. *Nat. Struct. Mol. Biol.* 24:931–943. https://doi.org/10.1038/nsmb.3483

Atherton, J., M. Stouffer, F. Francis, and C.A. Moores. 2018. Microtubule architecture in vitro and in cells revealed by cryo-electron tomography. *Acta Crystallogr. D Struct. Biol.* 74:572–584. https://doi.org/10.1107/S2059798318001948

Aumeier, C., L. Schaedel, J. Gaillard, K. John, L. Blanchoin, and M. Théry. 2016. Self-repair promotes microtubule rescue. *Nat. Cell Biol.* 18:1054–1064. https://doi.org/10.1038/ncb3406

Benoit, M.P.M.H., A.B. Asenjo, and H. Sosa. 2018. Cryo-EM reveals the structural basis of microtubule depolymerization by kinesin-13s. *Nat. Commun.* 9:1662. https://doi.org/10.1038/s41467-018-04044-8

Bergen, L.G., and G.G. Borisy. 1980. Head-to-tail polymerization of microtubules in vitro. Electron microscope analysis of seeded assembly. *J. Cell Biol.* 84:141–150. https://doi.org/10.1083/jcb.84.1.141

Bieling, P., L. Laan, H. Schek, E.L. Munteanu, L. Sandblad, M. Dogterom, D. Brunner, and T. Surrey. 2007. Reconstitution of a microtubule plus-end tracking system in vitro. *Nature.* 450:1100–1105. https://doi.org/10.1038/nature06386

Bowne-Anderson, H., M. Zanic, M. Kauer, and J. Howard. 2013. Microtubule dynamic instability: a new model with coupled GTP hydrolysis and multistep catastrophe. *BioEssays.* 35:452–461. https://doi.org/10.1002/bies.201200131

Brouhard, G.J., and L.M. Rice. 2018. Microtubule dynamics: an interplay of biochemistry and mechanics. *Nat. Rev. Mol. Cell Biol.* 19:451–463. https://doi.org/10.1038/s41580-018-0009-y

Cai, S., L.N. Weaver, S.C. Ems-McClung, and C.E. Walczak. 2009. Kinesin-14 family proteins HSET/XCTK2 control spindle length by cross-linking and sliding microtubules. *Mol. Biol. Cell.* 20:1348–1359. https://doi.org/10.1091/mbc.e08-09-0971

Caplow, M., and J. Shanks. 1996. Evidence that a single monolayer tubulin-GTP cap is both necessary and sufficient to stabilize microtubules. *Mol. Biol. Cell.* 7:663–675. https://doi.org/10.1091/mbc.7.4.663

Carlier, M.F., and D. Pantaloni. 1981. Kinetic analysis of guanosine 5′-triphosphate hydrolysis associated with tubulin polymerization. *Biochemistry.* 20:1918–1924. https://doi.org/10.1021/bi00510a030

Case, R.B., D.W. Pierce, N. Hom-Booher, C.L. Hart, and R.D. Vale. 1997. The directional preference of kinesin motors is specified by an element outside of the motor catalytic domain. *Cell.* 90:959–966. https://doi.org/10.1016/S0092-8674(00)80360-8

Castoldi, M., and A.V. Popov. 2003. Purification of brain tubulin through two cycles of polymerization-depolymerization in a high-molarity buffer. *Protein Expr. Purif.* 32:83–88. https://doi.org/10.1016/S1046-5928(03)00218-3

Chaaban, S., S. Jariwala, C.T. Hsu, S. Redemann, J.M. Kollman, T. Müller-Reichert, D. Sept, K.H. Bui, and G.J. Brouhard. 2018. The Structure and Dynamics of C. elegans Tubulin Reveals the Mechanistic Basis of Microtubule Growth. *Dev. Cell.* 47:191–204.e8. https://doi.org/10.1016/j.devcel.2018.08.023

Coombes, C.E., A. Yamamoto, M.R. Kenzie, D.J. Odde, and M.K. Gardner. 2013. Evolving tip structures can explain age-dependent microtubule catastrophe. *Curr. Biol.* 23:1342–1348. https://doi.org/10.1016/j.cub.2013.05.059

Dammermann, A., A. Desai, and K. Oegema. 2003. The minus end in sight. *Curr. Biol.* 13:R614–R624. https://doi.org/10.1016/S0960-9822(03)00530-X

Desai, A., and T.J. Mitchison. 1997. Microtubule polymerization dynamics. *Annu. Rev. Cell Dev. Biol.* 13:83–117. https://doi.org/10.1146/annurev.cellbio.13.1.83

Desai, A., S. Verma, T.J. Mitchison, and C.E. Walczak. 1999. Kin I kinesins are microtubule-destabilizing enzymes. *Cell.* 96:69–78. https://doi.org/10.1016/S0092-8674(00)80960-5

Domnitz, S.B., M. Wagenbach, J. Decarreau, and L. Wordeman. 2012. MCAK activity at microtubule tips regulates spindle microtubule length to promote robust kinetochore attachment. *J. Cell Biol.* 197:231–237. https://doi.org/10.1083/jcb.201108147

Drechsel, D.N., and M.W. Kirschner. 1994. The minimum GTP cap required to stabilize microtubules. *Curr. Biol.* 4:1053–1061. https://doi.org/10.1016/S0960-9822(00)00243-8

Drechsel, D.N., A.A. Hyman, M.H. Cobb, and M.W. Kirschner. 1992. Modulation of the dynamic instability of tubulin assembly by the microtubule-associated protein tau. *Mol. Biol. Cell.* 3:1141–1154. https://doi.org/10.1091/mbc.3.10.1141

Duellberg, C., N.I. Cade, D. Holmes, and T. Surrey. 2016. The size of the EB cap determines instantaneous microtubule stability. *eLife.* 5:e13470. https://doi.org/10.7554/eLife.13470

Fan, J., A.D. Griffiths, A. Lockhart, R.A. Cross, and L.A. Amos. 1996. Microtubule minus ends can be labelled with a phage display antibody specific to alpha-tubulin. *J. Mol. Biol.* 259:325–330. https://doi.org/10.1006/jmbi.1996.0322

Fees, C.P., and J.K. Moore. 2019. A unified model for microtubule rescue. *Mol. Biol. Cell.* 30:753–765. https://doi.org/10.1091/mbc.E18-08-0541

Fink, G., L. Hajdo, K.J. Skowronek, C. Reuther, A.A. Kasprzak, and S. Diez. 2009. The mitotic kinesin-14 Ncd drives directional microtubule-microtubule sliding. *Nat. Cell Biol.* 11:717–723. https://doi.org/10.1038/ncb1877

Fu, X., Y. Zhu, B. Zheng, Y. Zou, C. Wang, P. Wu, J. Wang, H. Chen, P. Du, B. Liang, and L. Fang. 2018. KIFC1, a novel potential prognostic factor and therapeutic target in hepatocellular carcinoma. *Int. J. Oncol.* 52: 1912–1922. https://doi.org/10.3892/ijo.2018.4348

Gardner, M.K., B.D. Charlebois, I.M. Jánosi, J. Howard, A.J. Hunt, and D.J. Odde. 2011a. Rapid microtubule self-assembly kinetics. *Cell.* 146: 582–592. https://doi.org/10.1016/j.cell.2011.06.053

Gardner, M.K., M. Zanic, C. Gell, V. Bormuth, and J. Howard. 2011b. Depolymerizing kinesins Kip3 and MCAK shape cellular microtubule architecture by differential control of catastrophe. *Cell.* 147:1092–1103. https://doi.org/10.1016/j.cell.2011.10.037

Gardner, M.K., M. Zanic, and J. Howard. 2013. Microtubule catastrophe and rescue. *Curr. Opin. Cell Biol.* 25:14–22. https://doi.org/10.1016/j.ceb.2012.09.006

Gell, C., V. Bormuth, G.J. Brouhard, D.N. Cohen, S. Diez, C.T. Friel, J. Helenius, B. Nitzsche, H. Petzold, J. Ribbe, et al. 2010. Microtubule dynamics reconstituted in vitro and imaged by single-molecule fluorescence microscopy. *Methods Cell Biol.* 95:221–245. https://doi.org/10.1016/S0091-679X(10)95013-9

Gell, C., C.T. Friel, B. Borgonovo, D.N. Drechsel, A.A. Hyman, and J. Howard. 2011. Purification of tubulin from porcine brain. *Methods Mol. Biol.* 777: 15–28. https://doi.org/10.1007/978-1-61779-252-6_2

Geyer, E.A., A. Burns, B.A. Lalonde, X. Ye, F.A. Piedra, T.C. Huffaker, and L.M. Rice. 2015. A mutation uncouples the tubulin conformational and GTPase cycles, revealing allosteric control of microtubule dynamics. *eLife.* 4:e10113. https://doi.org/10.7554/eLife.10113

Goodwin, S.S., and R.D. Vale. 2010. Patronin regulates the microtubule network by protecting microtubule minus ends. *Cell.* 143:263–274. https://doi.org/10.1016/j.cell.2010.09.022

Helenius, J., G. Brouhard, Y. Kalaidzidis, S. Diez, and J. Howard. 2006. The depolymerizing kinesin MCAK uses lattice diffusion to rapidly target microtubule ends. *Nature.* 441:115–119. https://doi.org/10.1038/nature04736

Hendershott, M.C., and R.D. Vale. 2014. Regulation of microtubule minus-end dynamics by CAMSAPs and Patronin. *Proc. Natl. Acad. Sci. USA.* 111: 5860–5865. https://doi.org/10.1073/pnas.1404133111

Hentrich, C., and T. Surrey. 2010. Microtubule organization by the antagonistic mitotic motors kinesin-5 and kinesin-14. *J. Cell Biol.* 189:465–480. https://doi.org/10.1083/jcb.200910125

Hepperla, A.J., P.T. Willey, C.E. Coombes, B.M. Schuster, M. Gerami-Nejad, M. McClellan, S. Mukherjee, J. Fox, M. Winey, D.J. Odde, et al. 2014. Minus-end-directed Kinesin-14 motors align antiparallel microtubules to control metaphase spindle length. *Dev. Cell.* 31:61–72. https://doi.org/10.1016/j.devcel.2014.07.023

Horio, T., and H. Hotani. 1986. Visualization of the dynamic instability of individual microtubules by dark-field microscopy. *Nature.* 321:605–607. https://doi.org/10.1038/321605a0

Hunter, A.W., M. Caplow, D.L. Coy, W.O. Hancock, S. Diez, L. Wordeman, and J. Howard. 2003. The kinesin-related protein MCAK is a microtubule depolymerase that forms an ATP-hydrolyzing complex at microtubule ends. *Mol. Cell.* 11:445–457. https://doi.org/10.1016/S1097-2765(03)00049-2

Hyman, A., D. Drechsel, D. Kellogg, S. Salser, K. Sawin, P. Steffen, L. Wordeman, and T. Mitchison. 1991. Preparation of modified tubulins. *Methods Enzymol.* 196:478–485. https://doi.org/10.1016/0076-6879(91)96041-O

Hyman, A.A., S. Salser, D.N. Drechsel, N. Unwin, and T.J. Mitchison. 1992. Role of GTP hydrolysis in microtubule dynamics: information from a slowly hydrolyzable analogue, GMPCPP. *Mol. Biol. Cell.* 3:1155–1167. https://doi.org/10.1091/mbc.3.10.1155

Jiang, K., S. Hua, R. Mohan, I. Grigoriev, K.W. Yau, Q. Liu, E.A. Katrukha, A.F.M. Altelaar, A.J.R. Heck, C.C. Hoogenraad, and A. Akhmanova. 2014. Microtubule minus-end stabilization by polymerization-driven CAMSAP deposition. *Dev. Cell.* 28:295–309. https://doi.org/10.1016/j.devcel.2014.01.001

Jiang, K., L. Rezabkova, S. Hua, Q. Liu, G. Capitani, A.F.M. Altelaar, A.J.R. Heck, R.A. Kammerer, M.O. Steinmetz, and A. Akhmanova. 2017. Microtubule minus-end regulation at spindle poles by an ASPM-katanin complex. *Nat. Cell Biol.* 19:480–492. https://doi.org/10.1038/ncb3511

Kuo, Y.-W., O. Trottier, M. Mahamdeh, and J. Howard. 2019. Spastin is a dual-function enzyme that severs microtubules and promotes their regrowth

to increase the number and mass of microtubules. *Proc. Natl. Acad. Sci. USA.* 116:5533–5541. https://doi.org/10.1073/pnas.1818824116

Kwon, M., S.A. Godinho, N.S. Chandhok, N.J. Ganem, A. Azioune, M. Thery, and D. Pellman. 2008. Mechanisms to suppress multipolar divisions in cancer cells with extra centrosomes. *Genes Dev.* 22:2189–2203. https://doi.org/10.1101/gad.1700908

Lawrence, E.J., and M. Zanic. 2019. Rescuing microtubules from the brink of catastrophe: CLASPs lead the way. *Curr. Opin. Cell Biol.* 56:94–101. https://doi.org/10.1016/j.ceb.2018.10.011

Lawrence, E.J., G. Arpağ, S.R. Norris, and M. Zanic. 2018. Human CLASP2 specifically regulates microtubule catastrophe and rescue. *Mol. Biol. Cell.* 29:1168–1177. https://doi.org/10.1091/mbc.E18-01-0016

Martin, M., and A. Akhmanova. 2018. Coming into focus: Mechanisms of microtubule minus-end organization. *Trends Cell Biol.* 28:574–588. https://doi.org/10.1016/j.tcb.2018.02.011

Martin, M., A. Veloso, J. Wu, E.A. Katrukha, and A. Akhmanova. 2018. Control of endothelial cell polarity and sprouting angiogenesis by non-centrosomal microtubules. *eLife.* 7:e33864. https://doi.org/10.7554/eLife.33864

Maurer, S.P., F.J. Fourniol, G. Bohner, C.A. Moores, and T. Surrey. 2012. EBs recognize a nucleotide-dependent structural cap at growing microtubule ends. *Cell.* 149:371–382. https://doi.org/10.1016/j.cell.2012.02.049

Maurer, S.P., N.I. Cade, G. Bohner, N. Gustafsson, E. Boutant, and T. Surrey. 2014. EB1 accelerates two conformational transitions important for microtubule maturation and dynamics. *Curr. Biol.* 24:372–384. https://doi.org/10.1016/j.cub.2013.12.042

Mickolajczyk, K.J., E.A. Geyer, T. Kim, L.M. Rice, and W.O. Hancock. 2019. Direct observation of individual tubulin dimers binding to growing microtubules. *Proc. Natl. Acad. Sci. USA.* 116:7314–7322. https://doi.org/10.1073/pnas.1815823116

Mitchison, T., and M. Kirschner. 1984. Dynamic instability of microtubule growth. *Nature.* 312:237–242. https://doi.org/10.1038/312237a0

Montenegro Gouveia, S., K. Leslie, L.C. Kapitein, R.M. Buey, I. Grigoriev, M. Wagenbach, I. Smal, E. Meijering, C.C. Hoogenraad, L. Wordeman, et al. 2010. In vitro reconstitution of the functional interplay between MCAK and EB3 at microtubule plus ends. *Curr. Biol.* 20:1717–1722. https://doi.org/10.1016/j.cub.2010.08.020

Moores, C.A., M. Yu, J. Guo, C. Beraud, R. Sakowicz, and R.A. Milligan. 2002. A mechanism for microtubule depolymerization by KinI kinesins. *Mol. Cell.* 9:903–909. https://doi.org/10.1016/S1097-2765(02)00503-8

Mountain, V., C. Simerly, L. Howard, A. Ando, G. Schatten, and D.A. Compton. 1999. The kinesin-related protein, HSET, opposes the activity of Eg5 and cross-links microtubules in the mammalian mitotic spindle. *J. Cell Biol.* 147:351–366. https://doi.org/10.1083/jcb.147.2.351

Newton, C.N., M. Wagenbach, Y. Ovechkina, L. Wordeman, and L. Wilson. 2004. MCAK, a Kin I kinesin, increases the catastrophe frequency of steady-state HeLa cell microtubules in an ATP-dependent manner in vitro. *FEBS Lett.* 572:80–84. https://doi.org/10.1016/j.febslet.2004.06.093

Nogales, E., S.G. Wolf, I.A. Khan, R.F. Ludueña, and K.H. Downing. 1995. Structure of tubulin at 6.5 A and location of the taxol-binding site. *Nature.* 375:424–427. https://doi.org/10.1038/375424a0

Nogales, E., S.G. Wolf, and K.H. Downing. 1998. Structure of the α β tubulin dimer by electron crystallography. *Nature.* 391:199–203. https://doi.org/10.1038/34465

Nogales, E., M. Whittaker, R.A. Milligan, and K.H. Downing. 1999. High-resolution model of the microtubule. *Cell.* 96:79–88. https://doi.org/10.1016/S0092-8674(00)80961-7

Noordstra, I., Q. Liu, W. Nijenhuis, S. Hua, K. Jiang, M. Baars, S. Remmelzwaal, M. Martin, L.C. Kapitein, and A. Akhmanova. 2016. Control of apico-basal epithelial polarity by the microtubule minus-end-binding protein CAMSAP3 and spectraplakin ACF7. *J. Cell Sci.* 129:4278–4288. https://doi.org/10.1242/jcs.194878

Norris, S.R., S. Jung, P. Singh, C.E. Strothman, A.L. Erwin, M.D. Ohi, M. Zanic, and R. Ohi. 2018. Microtubule minus-end aster organization is driven by processive HSET-tubulin clusters. *Nat. Commun.* 9:2659. https://doi.org/10.1038/s41467-018-04991-2

O'Brien, E.T., E.D. Salmon, R.A. Walker, and H.P. Erickson. 1990. Effects of magnesium on the dynamic instability of individual microtubules. *Biochemistry.* 29:6648–6656. https://doi.org/10.1021/bi00480a014

O'Toole, E.T., K.L. McDonald, J. Mäntler, J.R. McIntosh, A.A. Hyman, and T. Müller-Reichert. 2003. Morphologically distinct microtubule ends in the mitotic centrosome of *Caenorhabditis elegans.* *J. Cell Biol.* 163:451–456. https://doi.org/10.1083/jcb.200304035

Odde, D.J., L. Cassimeris, and H.M. Buettner. 1995. Kinetics of microtubule catastrophe assessed by probabilistic analysis. *Biophys. J.* 69:796–802. https://doi.org/10.1016/S0006-3495(95)79953-2

Ohi, R., K. Burbank, Q. Liu, and T.J. Mitchison. 2007. Nonredundant functions of Kinesin-13s during meiotic spindle assembly. *Curr. Biol.* 17:953–959. https://doi.org/10.1016/j.cub.2007.04.057

Oosawa, F. 1970. Size distribution of protein polymers. *J. Theor. Biol.* 27:69–86. https://doi.org/10.1016/0022-5193(70)90129-3

Pannu, V., P.C.G. Rida, A. Ogden, R.C. Turaga, S. Donthamsetty, N.J. Bowen, K. Rudd, M.V. Gupta, M.D. Reid, G. Cantuaria, et al. 2015. HSET overexpression fuels tumor progression via centrosome clustering-independent mechanisms in breast cancer patients. *Oncotarget.* 6:6076–6091. https://doi.org/10.18632/oncotarget.3475

Redemann, S., J. Baumgart, N. Lindow, M. Shelley, E. Nazockdast, A. Kratz, S. Prohaska, J. Brugués, S. Fürthauer, and T. Müller-Reichert. 2017. *C. elegans* chromosomes connect to centrosomes by anchoring into the spindle network. *Nat. Commun.* 8:15288. https://doi.org/10.1038/ncomms15288

Reinemann, D.N., S.R. Norris, R. Ohi, and M.J. Lang. 2018. Processive kinesin-14 HSET exhibits directional flexibility depending on motor traffic. *Curr. Biol.* 28:2356–2362.e5. https://doi.org/10.1016/j.cub.2018.06.055

Rickman, J., C. Duellberg, N.I. Cade, L.D. Griffin, and T. Surrey. 2017. Steady-state EB cap size fluctuations are determined by stochastic microtubule growth and maturation. *Proc. Natl. Acad. Sci. USA.* 114:3427–3432. https://doi.org/10.1073/pnas.1620274114

Sanchez, A.D., and J.L. Feldman. 2017. Microtubule-organizing centers: from the centrosome to non-centrosomal sites. *Curr. Opin. Cell Biol.* 44:93–101. https://doi.org/10.1016/j.ceb.2016.09.003

Schindelin, J., I. Arganda-Carreras, E. Frise, V. Kaynig, M. Longair, T. Pietzsch, S. Preibisch, C. Rueden, S. Saalfeld, B. Schmid, et al. 2012. Fiji: an open-source platform for biological-image analysis. *Nat. Methods.* 9:676–682. https://doi.org/10.1038/nmeth.2019

Seetapun, D., B.T. Castle, A.J. McIntyre, P.T. Tran, and D.J. Odde. 2012. Estimating the microtubule GTP cap size in vivo. *Curr. Biol.* 22:1681–1687. https://doi.org/10.1016/j.cub.2012.06.068

Sproul, L.R., D.J. Anderson, A.T. Mackey, W.S. Saunders, and S.P. Gilbert. 2005. Cik1 targets the minus-end kinesin depolymerase kar3 to microtubule plus ends. *Curr. Biol.* 15:1420–1427. https://doi.org/10.1016/j.cub.2005.06.066

Tanaka, N., W. Meng, S. Nagae, and M. Takeichi. 2012. Nezha/CAMSAP3 and CAMSAP2 cooperate in epithelial-specific organization of non-centrosomal microtubules. *Proc. Natl. Acad. Sci. USA.* 109:20029–20034. https://doi.org/10.1073/pnas.1218017109

Ti, S.C., M.C. Pamula, S.C. Howes, C. Duellberg, N.I. Cade, R.E. Kleiner, S. Forth, T. Surrey, E. Nogales, and T.M. Kapoor. 2016. Mutations in human tubulin proximal to the kinesin-binding site alter dynamic instability at microtubule plus- and minus-ends. *Dev. Cell.* 37:72–84. https://doi.org/10.1016/j.devcel.2016.03.003

Tran, P.T., R.A. Walker, and E.D. Salmon. 1997. A metastable intermediate state of microtubule dynamic instability that differs significantly between plus and minus ends. *J. Cell Biol.* 138:105–117. https://doi.org/10.1083/jcb.138.1.105

Trinczek, B., A. Marx, E.M. Mandelkow, D.B. Murphy, and E. Mandelkow. 1993. Dynamics of microtubules from erythrocyte marginal bands. *Mol. Biol. Cell.* 4:323–335. https://doi.org/10.1091/mbc.4.3.323

Vemu, A., E. Szczesna, E.A. Zehr, J.O. Spector, N. Grigorieff, A.M. Deaconescu, and A. Roll-Mecak. 2018. Severing enzymes amplify microtubule arrays through lattice GTP-tubulin incorporation. *Science.* 361:eaau1504. https://doi.org/10.1126/science.aau1504

von Loeffelholz, O., N.A. Venables, D.R. Drummond, M. Katsuki, R. Cross, and C.A. Moores. 2017. Nucleotide- and Mal3-dependent changes in fission yeast microtubules suggest a structural plasticity view of dynamics. *Nat. Commun.* 8:2110. https://doi.org/10.1038/s41467-017-02241-5

Voter, W.A., E.T. O'Brien, and H.P. Erickson. 1991. Dilution-induced disassembly of microtubules: relation to dynamic instability and the GTP cap. *Cell Motil. Cytoskeleton.* 18:55–62. https://doi.org/10.1002/cm.970180106

Walczak, C.E., T.J. Mitchison, and A. Desai. 1996. XKCM1: a Xenopus kinesin-related protein that regulates microtubule dynamics during mitotic spindle assembly. *Cell.* 84:37–47. https://doi.org/10.1016/S0092-8674(00)80991-5

Walker, R.A., E.T. O'Brien, N.K. Pryer, M.F. Soboeiro, W.A. Voter, H.P. Erickson, and E.D. Salmon. 1988. Dynamic instability of individual microtubules analyzed by video light microscopy: rate constants and transition frequencies. *J. Cell Biol.* 107:1437–1448. https://doi.org/10.1083/jcb.107.4.1437

Walker, R.A., S. Inoué, and E.D. Salmon. 1989. Asymmetric behavior of severed microtubule ends after ultraviolet-microbeam irradiation of individual microtubules in vitro. *J. Cell Biol.* 108:931–937. https://doi.org/10.1083/jcb.108.3.931

Walker, R.A., N.K. Pryer, and E.D. Salmon. 1991. Dilution of individual microtubules observed in real time in vitro: evidence that cap size is small and independent of elongation rate. *J. Cell Biol.* 114:73–81. https://doi.org/10.1083/jcb.114.1.73

Wordeman, L., and T.J. Mitchison. 1995. Identification and partial characterization of mitotic centromere-associated kinesin, a kinesin-related protein that associates with centromeres during mitosis. *J. Cell Biol.* 128:95–104. https://doi.org/10.1083/jcb.128.1.95

Wu, J., K. Mikule, W. Wang, N. Su, P. Petteruti, F. Gharahdaghi, E. Code, X. Zhu, K. Jacques, Z. Lai, et al. 2013. Discovery and mechanistic study of a small molecule inhibitor for motor protein KIFC1. *ACS Chem. Biol.* 8:2201–2208. https://doi.org/10.1021/cb400186w

Xiao, Y.-X., and W.-X. Yang. 2016. KIFC1: a promising chemotherapy target for cancer treatment? *Oncotarget.* 7:48656–48670. https://doi.org/10.18632/oncotarget.8799

Yau, K.W., S.F.B. van Beuningen, I. Cunha-Ferreira, B.M.C. Cloin, E.Y. van Battum, L. Will, P. Schätzle, R.P. Tas, J. van Krugten, E.A. Katrukha, et al. 2014. Microtubule minus-end binding protein CAMSAP2 controls axon specification and dendrite development. *Neuron.* 82:1058–1073. https://doi.org/10.1016/j.neuron.2014.04.019

Yvon, A.M., and P. Wadsworth. 1997. Non-centrosomal microtubule formation and measurement of minus end microtubule dynamics in A498 cells. *J. Cell Sci.* 110:2391–2401. https://doi.org/10.1083/jcb.114.1.73

Zanic, M. 2016. Measuring the effects of microtubule-associated proteins on microtubule dynamics in vitro. *Methods Mol. Biol.* 1413:47–61. https://doi.org/10.1007/978-1-4939-3542-0_4

Zanic, M., J.H. Stear, A.A. Hyman, and J. Howard. 2009. EB1 recognizes the nucleotide state of tubulin in the microtubule lattice. *PLoS One.* 4:e7585. https://doi.org/10.1371/journal.pone.0007585

Zhang, R., G.M. Alushin, A. Brown, and E. Nogales. 2015. Mechanistic origin of microtubule dynamic instability and its modulation by EB proteins. *Cell.* 162:849–859. https://doi.org/10.1016/j.cell.2015.07.012

Zhang, R., J. Roostalu, T. Surrey, and E. Nogales. 2017. Structural insight into TPX2-stimulated microtubule assembly. *eLife.* 6:e30959. https://doi.org/10.7554/eLife.30959

Zhang, R., B. LaFrance, and E. Nogales. 2018. Separating the effects of nucleotide and EB binding on microtubule structure. *Proc. Natl. Acad. Sci. USA.* 115:E6191–E6200. https://doi.org/10.1073/pnas.1802637115